

\mathcal{PT} -symmetric Talbot effect in a temporal mesh latticeShulin Wang,¹ Bing Wang,^{1,*} and Peixiang Lu^{1,2,†}¹*School of Physics and Wuhan National Laboratory for Optoelectronics, Huazhong University of Science and Technology, Wuhan 430074, China*²*Laboratory for Optical Information Technology, Wuhan Institute of Technology, Wuhan 430205, China*

(Received 28 August 2018; published 15 October 2018)

We investigate the \mathcal{PT} -symmetric Talbot effect in a temporal mesh lattice constructed by two coupled fiber loops, in which the \mathcal{PT} symmetry is introduced through temporally controlling the gain and loss of the loops. The Talbot self-imaging exists only if the period of input pulse train is chosen as two- or fourfold compared to the time interval caused by the length difference between the two loops. Through varying the gain and loss, we can tailor the lattice band structure and thus flexibly manipulate the Talbot distance, which can further be tuned by imposing a linear phase distribution on the input pulse train. In addition, the power oscillations are found in the Talbot imaging process, and the oscillation amplitude is associated with the gain and loss and the gradient of the linear phase modulation. Especially, the power oscillations possess significant amplitude as the modes near the exceptional points are excited. The study may find potential applications in pulse repetition rate multiplication, temporal cloaking, and tunable intensity amplifiers.

DOI: [10.1103/PhysRevA.98.043832](https://doi.org/10.1103/PhysRevA.98.043832)**I. INTRODUCTION**

The non-Hermitian Hamiltonians possess entirely real spectra as they respect parity-time (\mathcal{PT}) symmetry, which was demonstrated by Bender and co-workers in 1998 [1,2]. The \mathcal{PT} symmetry demands that the complex potential has a symmetric distribution of the real part and an antisymmetric distribution of the imaginary part. Optical systems have been considered as ideal platforms to realize \mathcal{PT} symmetry, where the gain and loss play the role of the imaginary part of the potential [3–14]. Compared to the passive systems, the optical structures with \mathcal{PT} symmetry have some extraordinary characteristics, such as power oscillations [3,6,8], the breaking of refraction symmetry [3,15], and unidirectional invisibility [11,12]. The \mathcal{PT} symmetry in optics is firstly observed in two coupled waveguides [5,7], but it is practically difficult to fabricate a large-scale optical lattice with \mathcal{PT} symmetry. Recently, the concept of the lattice has been generalized from real space to synthetic dimensions [16–29], such as temporal and spectral lattices. These synthetic lattices provide feasible platforms to study \mathcal{PT} symmetry in practice [18,19,22,29]. The temporal mesh lattice, as a representative, is proposed by drawing an analogy between the pulse evolution in two coupled fiber loops and the beam dynamics in spatial mesh lattice. Through the temporal control of the gain and loss in the loops, the \mathcal{PT} symmetry in a large-scale lattice is firstly carried out in experiment [19].

On the other hand, the Talbot effect is a traditional optical phenomenon of self-imaging, which can be explained satisfactorily by the Fresnel theory [30–34]. The revival distance, termed the Talbot distance, is related to the input

wavelength and period. Considering the space-time duality between diffraction and dispersion, the temporal Talbot effect is proposed to achieve the reconstruction of the periodic pulse train or increase the repetition rate of the incident pulse train [35,36]. The temporal Talbot recurrence has found many applications in optical communication, such as pulse repetition rate multiplication [37–40], temporal cloaking [41–43], and noiseless amplification [44]. Apart from a continuous medium, Talbot self-imaging has also been extended to discrete systems [45–53], such as waveguide arrays [46–53]. Differing from the continuous Talbot effect which is period independent, the Talbot revival in waveguide arrays exists only for input periods of 1, 2, 3, 4, or 6 [46,47,49,51]. In addition, the \mathcal{PT} -symmetric Talbot effect is firstly proposed by introducing balanced gain and loss to these arrays. The input periods allowing Talbot effect are 1, 2, and 3; meanwhile, the gain and loss parameter provides a new degree of freedom to manipulate the Talbot distance [54]. Considering the fabrication difficulties, the temporal mesh lattice may be a more accessible platform to realize the \mathcal{PT} -symmetric Talbot effect.

In this work, we shall investigate the \mathcal{PT} -symmetric Talbot effect in the temporal mesh lattice constructed by two coupled fiber loops. The Talbot self-imaging can be supported below, at, and even above the \mathcal{PT} transition threshold. Unlike the continuous Talbot effect, the Talbot recurrence in such discrete lattice exists only if the period of incident pulse train is chosen from certain specific values. The enumeration method is employed to find the input periods allowing the Talbot effect. Moreover, the lattice band structure can be tailored by controlling the gain and loss, providing possibilities to manipulate the Talbot distance. The Talbot distance could further be tuned by imposing a linear phase modulation on the input pulse train, which is also discussed in detail. Differing from the temporal Talbot effect in the passive systems, the pulse train manifests power oscillations in the Talbot process

*wangbing@hust.edu.cn

†lupeixiang@hust.edu.cn

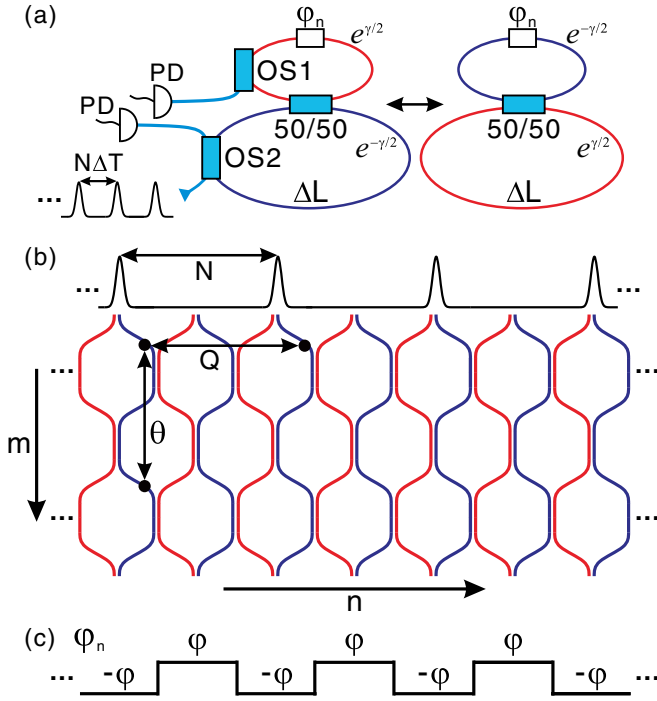


FIG. 1. (a) Schematic of two coupled fiber loops. The red (purple) loop has a gain factor of $e^{\gamma/2}$ ($e^{-\gamma/2}$), and both loops change between gain and loss alternately after every round trip. OS1 and OS2 are optical switches, through which we inject the periodic pulse train to the long loop and couple out the pulse sequences from the loops. PD denotes photodiode. (b) Schematic of temporal mesh lattice with \mathcal{PT} symmetry. The pulse train is amplified in the red path and attenuated in the purple path, which mimics the antisymmetric distribution of the imaginary part of the complex potential. (c) Distribution of the phase modulation φ_n .

due to the mode nonorthogonality. Moreover, the oscillation amplitude is associated with both the gain and loss and the gradient of the linear phase modulation.

II. STRUCTURE AND MODEL

Figure 1(a) shows the coupled fiber-loop circuit that constructs the temporal mesh lattice with \mathcal{PT} symmetry. Two fiber loops with a length difference ΔL are connected by a 50:50 directional coupler. The time interval caused by the length difference is $2\Delta T = \Delta L/c_F$, where c_F is the light speed in the fiber. A periodic pulse train is injected into the long loop. After passing through the coupler, two new pulse sequences are generated and flow into two loops. A round trip later, the pulse train in the short loop is advanced compared to the one in the long loop, and then two pulse trains will interfere at the coupler. The pulse sequences evolve in stepwise manner with the increase of round-trip number, which is an analogy of the beam dynamics in the spatial mesh lattice [19,45]. The equivalent mesh lattice in the time domain is illustrated in Fig. 1(b), where m is the times the pulse trains enter the coupler, and n is the relative position of the pulse in the train. To ensure the complex potential have an antisymmetric distribution of the imaginary part, the gain and loss are under the temporal control, and the gain factor of each

loop changes between $e^{\gamma/2}$ and $e^{-\gamma/2}$ alternately, where γ is the gain and loss factor. The symmetric distribution of the real part is accomplished by applying a phase modulation in the short loop. We denote the complex amplitudes of pulses in the short and long loops as u_n^m and v_n^m , respectively. The pulse dynamics reads

$$\begin{aligned} u_n^m &= \frac{1}{\sqrt{2}} e^{(-1)^m \gamma/2} (u_{n+1}^{m-1} + i v_{n+1}^{m-1}), \\ v_n^m &= \frac{1}{\sqrt{2}} e^{(-1)^{m+1} \gamma/2} (i u_{n-1}^{m-1} + v_{n-1}^{m-1}) e^{i\varphi_n}, \end{aligned} \quad (1)$$

in which φ_n is the function of the phase modulation [18,19]. φ_n could be denoted as

$$\varphi_n = \begin{cases} \varphi (n = 4K, 4K + 3) \\ -\varphi (n = 4K + 1, 4K + 2) \end{cases}, \quad (2)$$

where φ is the amplitude of the phase modulation, and $K \in \mathbb{Z}$. The distribution of φ_n is depicted in Fig. 1(c). The Bloch mode in such lattice is

$$\begin{pmatrix} u_n^m \\ v_n^m \end{pmatrix} = \begin{pmatrix} U_0 \\ V_0 \end{pmatrix} e^{iQn/4} e^{i\theta m/2}, \quad (3)$$

where $(U_0, V_0)^T$ is the eigenvector; Q and θ are the transverse Bloch momentum and longitudinal propagation constant, respectively [18,19]. By inserting Eqs. (2) and (3) into Eq. (1), the band structure is obtained and reads

$$\begin{aligned} \cos Q &= 8 \cos^2 \theta - 8 \cosh \gamma \cos \varphi \cos \theta \\ &+ 4 \cos^2 \varphi - 4 + \cosh(2\gamma). \end{aligned} \quad (4)$$

The \mathcal{PT} transition threshold [18,19] is given by

$$\gamma_{PT} = \min\{\cosh^{-1}[2 \cos \varphi - \sqrt{\cos(2\varphi)}]; \cosh^{-1}(\sqrt{2})\}. \quad (5)$$

As $\varphi = \pi/2$, the band structure is simplified greatly, which can be expressed as

$$\cos Q = 8 \cos^2 \theta - 4 + \cosh(2\gamma). \quad (6)$$

The \mathcal{PT} transition threshold is $\gamma_{PT} = 0.88$ according to Eq. (5). The band structures with various gain and loss factors are depicted in Fig. 2. As $\gamma < \gamma_{PT}$, the band structures shown in Figs. 2(a) and 2(b) are completely real. For $\gamma = \gamma_{PT}$, the exceptional points (EPs) arise at the edges of the Brillouin zone [19,55,56], as shown in Fig. 2(c). As $\gamma_{PT} < \gamma < \gamma_{IM}$, the band structure is partially complex [Fig. 2(d)], where $\gamma_{IM} = 1.15$. As $\gamma > \gamma_{IM}$, the imaginary part becomes nonzero at whole band structure, as shown in Figs. 2(e) and 2(f). In addition, the band structures are symmetric in θ , and the symmetric axis is the Q axis. The two bands are also symmetric, and the symmetric axes are $\theta = \pm\pi/2$.

We consider the necessary condition that guarantees the existence of the Talbot effect in such lattice. As shown in Fig. 1(b), the input field has a period of N in the temporal mesh lattice. Due to the discreteness in the transverse direction, N is an integer. Accordingly, the incident pulse sequence has a period of $N\Delta T$ in the coupled loops. To meet the periodic boundary condition, the Bloch momentum should be in the form of $Q_l = 2\pi l/\mathcal{N}$, where $\mathcal{N} = N/4$, and $l = 0, 1, \dots, \mathcal{N} - 1$. For modes with Q_l , the corresponding propagation

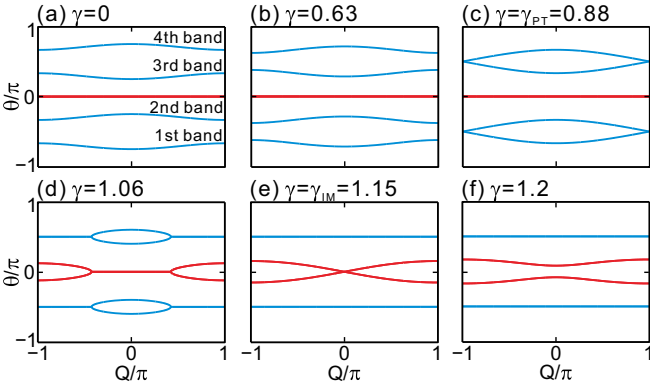


FIG. 2. (a)–(f) Band structures for $\gamma = 0, 0.63, 0.88, 1.06, 1.15,$ and $1.2,$ respectively. The blue and red lines represent the real and imaginary parts of the propagation constant, respectively.

constants could be denoted as $\theta_{j,l}$, where j is the band index and is equal to 1, 2, 3, and 4. The propagation constant at the third band is

$$\theta_{3,l} = \arccos[\sqrt{8 + 2 \cos Q_l - 2 \cos(2\gamma)}/4]. \quad (7)$$

Due to the symmetric properties of the band structure, the propagation constants at the first, second, and fourth bands are $\theta_{1,l} = -\pi + \theta_{3,l}$, $\theta_{2,l} = -\theta_{3,l}$, and $\theta_{4,l} = \pi - \theta_{3,l}$, respectively. The field evolution can be expressed as a superposition of Bloch modes,

$$\begin{pmatrix} u_n^m \\ v_n^m \end{pmatrix} = \sum_{j=1}^4 \sum_{l=0}^{N-1} c_{j,l} \begin{pmatrix} U_{j,l} \\ V_{j,l} \end{pmatrix} \exp(i Q_l n/4) \exp(i \theta_{j,l} m/2), \quad (8)$$

where $(U_{j,l} \ V_{j,l})^T$ and $c_{j,l}$ are the eigenvector and coefficient, respectively. All modes contained in the field evolution should be able to exhibit a revival to realize the Talbot effect. For a component with $\theta_{j,l}$, the revival exists only if $\theta_{j,l}$ satisfies

$$\lambda_{j,l} \theta_{j,l}/2 = 2\mu_{j,l}\pi, \quad (9)$$

where $\lambda_{j,l}$ is the revival distance or the effective wavelength; $\mu_{j,l}$ is a nonzero integer. $\lambda_{j,l}$ is also an integer because the temporal mesh lattice is discrete in the propagation direction. As a result, $\theta_{j,l}$ should be a rational multiple of π . The Talbot distance is

$$z_T = \text{LCM}(\lambda_{1,0}, \lambda_{1,1}, \dots, \lambda_{1,N}, \lambda_{2,0}, \dots, \lambda_{4,N}), \quad (10)$$

where LCM is the least common multiple.

III. RESULTS AND DISCUSSIONS

A. Talbot effect below \mathcal{PT} transition threshold

We now focus on the Talbot effect below the \mathcal{PT} transition threshold. For $N = 4$, the Bloch momentum takes a value of $Q_0 = 0$ considering the periodic boundary condition. The propagation constant at the third band is

$$\theta_{3,0} = \arccos[\sqrt{10 - 2 \cos(2\gamma)}/4]. \quad (11)$$

The corresponding propagation constants at the other bands are $\theta_{1,0} = -\pi + \theta_{3,0}$, $\theta_{2,0} = -\theta_{3,0}$, and $\theta_{4,0} = \pi - \theta_{3,0}$.

The Talbot effect will be supported as the mode with $\theta_{3,0}$ could exhibit recurrence during propagation. To illustrate the above statement, we firstly assume that the revival of the mode with $\theta_{3,0}$ is valid. $\theta_{3,0}$ has to satisfy Eq. (10) and thus be a rational multiple of π . We denote $\theta_{3,0}$ as $p\pi/q$, in which p and q are the relative prime positive integers. Considering the symmetric properties of the band structure, the propagation constants at the other bands are $\theta_{1,0} = -\pi + p\pi/q$, $\theta_{2,0} = -p\pi/q$, and $\theta_{4,0} = \pi - p\pi/q$. $\theta_{1,0}$, $\theta_{2,0}$, and $\theta_{4,0}$ are all rational multiples of π , which enables the existence of the Talbot effect. For odd p and odd q , the revival distances of the modes with $\theta_{1,0}$, $\theta_{2,0}$, $\theta_{3,0}$, and $\theta_{4,0}$ are $\lambda_{1,0} = 2q$, $\lambda_{2,0} = 4q$, $\lambda_{3,0} = 4q$, and $\lambda_{4,0} = 2q$, respectively. The Talbot distance is thus $z_T = 4q$ which is the LCM of $2q$ and $4q$. For odd p and odd q or even p and odd q , the Talbot distance is still $z_T = 4q$. The gain and loss parameter γ could be derived from Eq. (11), which can be expressed as

$$\gamma = \text{arccosh}\sqrt{3 - 4\cos^2\theta_{3,0}}. \quad (12)$$

Due to $0 \leq \gamma < 0.88$, $\theta_{3,0}$ belongs to $[\pi/4, \pi/3)$. q is thus 4 at least, corresponding to the Talbot distance of $z_T = 16$. Considering the existence of noises, the longest valid propagation distance is about $M_L = 400$ steps according to the experimental works reported in [20,26]. The set of available Talbot distances is $\{16, 20, 24, \dots, 4q, \dots, M_L\}$. We show the Talbot distance z_T varying with γ in Fig. 3(a). For $\gamma = 0$, the propagation constant at the third band is $\theta_{3,0} = \pi/4$, and the Talbot distance is $z_T = 16$. The pulse intensity evolution or the Talbot carpet is shown in Fig. 3(b) where the incident pulse train exhibits revival after every 16 steps. Note that the pulse train at $m = 8$ has the same intensity distribution with the initial one, but it accumulates a phase delay of π from $m = 0$ to $m = 8$. For $\gamma = 0.63$, the Talbot distance is $z_T = 28$ as $\theta_{3,0} = 2\pi/7$, and the Talbot carpet shown in Fig. 3(c) coincides well with the theoretical analysis.

For $N = 8$, the modes with $Q_0 = 0$ and $Q_1 = \pi$ are contained in the field evolution. The propagation constants at the third band are

$$\begin{aligned} \theta_{3,0} &= \arccos[\sqrt{10 - 2 \cosh(2\gamma)}/4], \\ \theta_{3,1} &= \arccos[\sqrt{6 - 2 \cosh(2\gamma)}/4]. \end{aligned} \quad (13)$$

We use the enumeration method to study the existence of the Talbot effect. To support the revivals, $\theta_{3,0}$ and $\theta_{3,1}$ should both be in the form of $p\pi/q$, corresponding to the revival distance $2q$ (even p) or $4q$ (odd p). Considering the longest valid distance M_L , q is no more than $M_L/2$. Due to $4 \leq q \leq M_L/2$ and $q/4 \leq p < q/3$, $\theta_{3,0}$ and $\theta_{3,1}$ are from a finite set, which enables the enumeration method [45]. It turns out that the Talbot effect occurs only if γ is chosen as 0. The corresponding Talbot distance is $z_T = 48$, as illustrated in Fig. 3(d). As $N > 8$, we also employ the enumeration method to find the allowed values of N and γ . Considering the longest valid propagation distance M_L , N is no more than $2M_L$. Otherwise, the adjacent pulses will exhibit ballistic spreading separately within M_L [19]. Due to the periodic incidence condition and the discreteness in the transverse direction, the set of N should be $\{4, 8, 12, \dots, 2M_L\}$. After enumerating the set of N , it turns out that the Talbot effect is not preserved as $N > 8$. For $N = 12$, the pulse intensity evolution is shown in

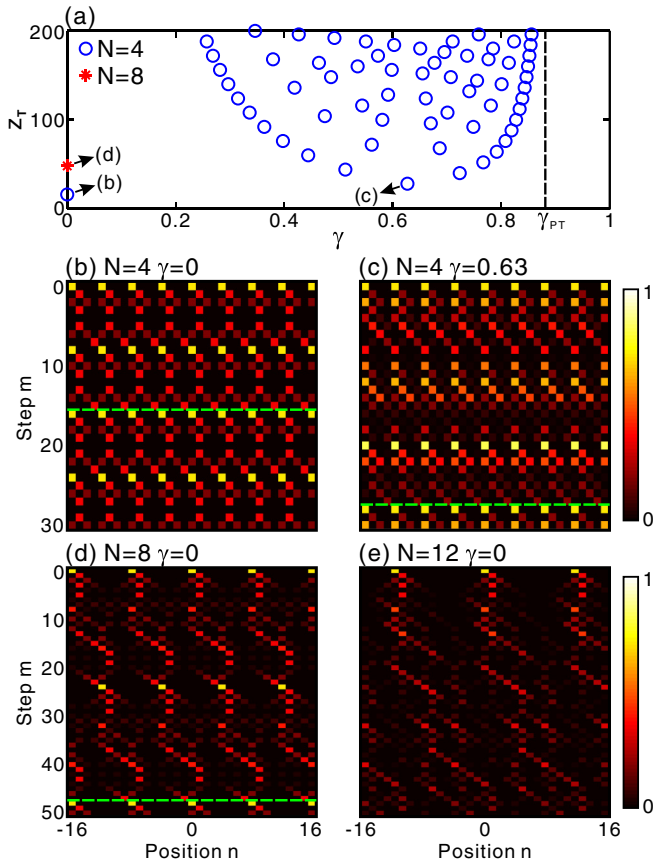


FIG. 3. (a) Talbot distance z_T versus γ below the \mathcal{PT} transition threshold. (b), (c) Pulse intensity evolutions in the long loop for $\gamma = 0$ and $\gamma = 0.63$, respectively. The input period is chosen as $N = 4$. (d), (e) Pulse intensity evolutions in the long loop for $N = 8$ and $N = 12$. γ is chosen as 0. The green dotted lines denote the locations of the Talbot images.

Fig. 3(e) where the spreading pattern is not periodic along the propagation direction.

The fractional temporal Talbot effect also exists in the \mathcal{PT} -symmetric mesh lattice [45]. The repetition rate of the pulse train could be increased two- or fourfold compared to the initial one in the Talbot process, as shown in Figs. 2(b)–2(d). The fractional Talbot effect here could find applications in pulse repetition rate multiplication and temporal cloaking [40,43]. Specifically, as the pulse sequence propagates from the integer to the fractional Talbot distance, the pulse repetition rate is scaled up by two or four times, which can be applied to the pulse repetition rate multiplication [40]. From the fractional to the integer Talbot distance, the pulse repetition rate is scaled down by two or four times with the time gap between adjacent pulses increased. The enlarged time gap will be more beneficial to the realization of temporal cloaking within which an event could be hidden from being detected [43].

The Talbot distance can also be manipulated by imposing a linear phase modulation on the incident pulse train. We denote the interval between the phase shifts on the adjacent pulses as ϕ_0 . Accordingly, the input field of the temporal mesh lattice has an initial momentum ϕ_0 [Fig. 4(a)], which leads to the Bloch momentum taking the value from a set of

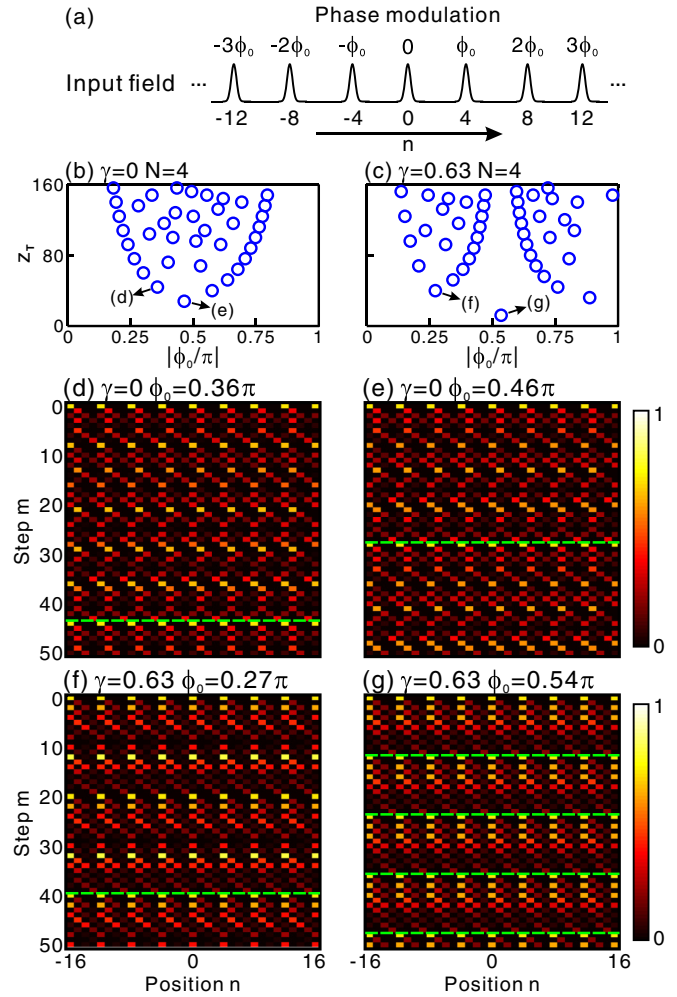


FIG. 4. (a) Schematic of the linear phase modulation imposed on the input field. (b), (c) Talbot distance z_T versus $|\phi_0|$ for $\gamma = 0$ and 0.63, respectively. The incident period is $N = 4$. (d), (e) Talbot carpets for $\phi_0 = 0.36\pi$ and $\phi_0 = 0.46\pi$, respectively. γ is set as 0. (f), (g) Talbot carpets for $\phi_0 = 0.27\pi$ and $\phi_0 = 0.54\pi$, respectively. γ is chosen as 0.63.

$Q_l = 2\pi l/\mathcal{N} + \phi_0$. For $N = 4$, the corresponding propagation constant at the third band is

$$\theta_{3,0} = \arccos[\sqrt{2 \cos \phi_0 + 8 - 2 \cosh(2\gamma)}/4]. \quad (14)$$

The Talbot effect exists only if $\theta_{3,0}$ is a rational multiple of π . We denote $\theta_{3,0}$ as $\theta_{3,0} = a\pi/b$, where a and b are the relative prime positive integers. The Talbot distance is $z_T = 4b$. Due to $-\pi \leq \phi_0 \leq \pi$ and $0 \leq \gamma < 0.88$, $\theta_{3,0}$ should belong to $[\pi/4, \pi/2)$. b is thus 3 at least, corresponding to the Talbot distance of $z_T = 12$. The set of available Talbot distances is $\{12, 16, 20, \dots, 4b, \dots, M_L\}$. ϕ_0 can be derived from Eq. (14), which is expressed as

$$\phi_0 = \arccos[8 \cos^2 \theta_{3,0} - 4 + \cosh(2\gamma)]. \quad (15)$$

We show the Talbot distance z_T varying with ϕ_0 in Figs. 4(b) and 4(c). For $\gamma = 0$, the Talbot distances are $z_T = 44$ and $z_T = 28$ as $\phi_0 = 0.36\pi$ and $\phi_0 = 0.46\pi$. For $\gamma = 0.63$, the corresponding Talbot distances are $z_T = 40$ and $z_T = 12$ for $\phi_0 = 0.27\pi$ and $\phi_0 = 0.54\pi$. The Talbot

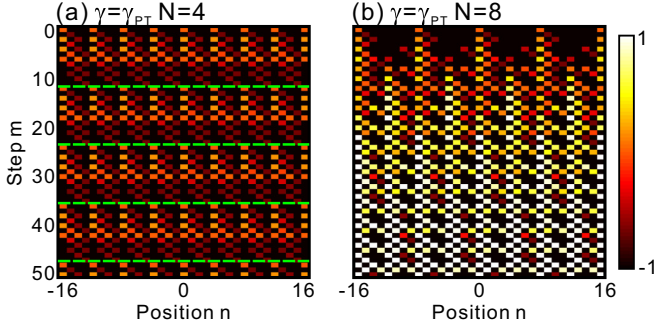


FIG. 5. (a), (b) Pulse intensity evolutions (after log transformation) for $N = 4$ and 8 at the \mathcal{PT} transition threshold.

carpets shown in Figs. 4(d)–4(g) agree well with the above theoretical analysis. For $N = 8$, the modes with $Q_0 = \phi_0$ and $Q_1 = \pi + \phi_0$ are contained in the field evolution. The propagation constants at the third band are

$$\begin{cases} \theta_{3,0} = \arccos[\sqrt{2 \cos \phi_0 + 8 - 2 \cosh(2\gamma)}/4], \\ \theta_{3,1} = \arccos[\sqrt{-2 \cos \phi_0 + 8 - 2 \cosh(2\gamma)}/4]. \end{cases} \quad (16)$$

The Talbot self-imaging is not preserved in the presence of the nonzero phase modulation, which is obtained from the enumeration method. In addition, we consider the influences of dispersion. At arbitrary step m , all pulses almost propagate the same distances in the fiber loops. They are influenced by the dispersion equally. As a result, the repetition rate of the pulse train does not change while the pulse width is broadened.

B. Talbot effect at \mathcal{PT} transition threshold

The Talbot effect also occurs at the \mathcal{PT} transition threshold. For $N = 4$, the propagation constant at the third band is $\theta_{3,0} = \pi/3$, and thus the Talbot distance is $z_T = 12$. The Talbot carpet is illustrated in Fig. 5(a). For $N = 8$, the modes with $Q_0 = 0$ and $Q_1 = \pi$ are included in the field evolution. The propagation constants at the third band are $\theta_{3,0} = \pi/3$ and $\theta_{3,1} = \pi/2$. It is supposed that the Talbot revivals should exist because $\theta_{3,0}$ and $\theta_{3,1}$ are both rational multiples of π . Contrary to expectation, the Talbot recurrence fails, and the total energy of the pulse train increases almost linearly along the propagation direction [Fig. 5(b)]. The reason is that the modes with $Q_1 = \pi$ are excited at the EPs, where the mode degeneracy occurs [3,8]. For $N > 8$, we investigate the existence of the Talbot effect by the enumeration method. It turns out that the Talbot effect is not supported in such cases.

The Talbot distance can also be manipulated by applying a linear phase modulation to the incident pulse sequence. For $N = 4$, the Bloch momentum is $Q_0 = \phi_0$, and the propagation constant at the third band is

$$\theta_{3,0} = \arccos[\sqrt{2 \cos \phi_0 + 2}/4]. \quad (17)$$

The Talbot effect exists only if $\theta_{3,0}$ is a rational multiple of π except the case where the modes at EPs are excited. $\theta_{3,0}$ should also be in the form of $\theta_{3,0} = a\pi/b$, and the Talbot distance is $z_T = 4b$. Considering $\pi/3 \leq \theta_{3,0} < \pi/2$, b is 3 at least. The set of available Talbot distances is $\{12, 16, 20, \dots,$

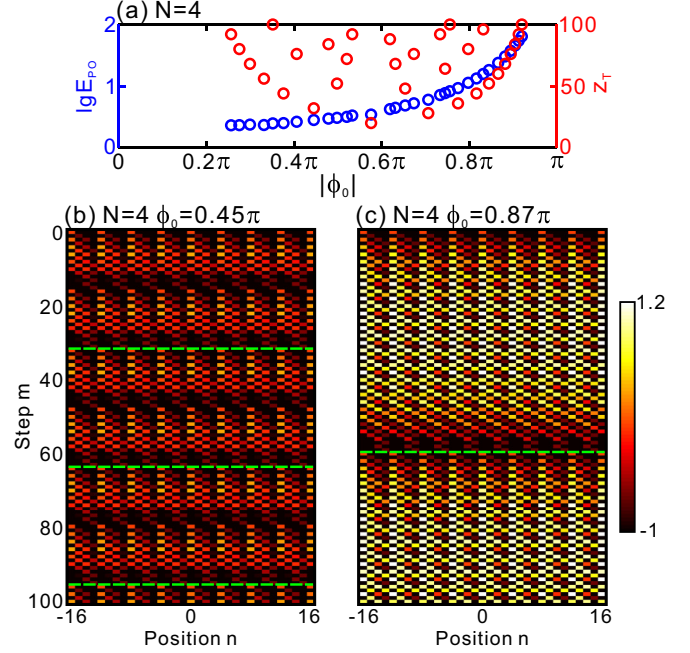


FIG. 6. (a) Talbot distance z_T and oscillation amplitude E_{PO} (after log transformation) varying with $|\phi_0|$. (b), (c) Pulse intensity evolutions (after log transformation) with ϕ_0 being 0.45π and 0.87π , respectively. The incident period is $N = 4$.

$4b, \dots, M_L\}$, as illustrated in Fig. 6(a). Meanwhile, significant power oscillations occur as the modes included are excited near the EPs due to the nonorthogonality of modes [3,8]. The oscillation amplitude E_{PO} is obtained by calculating the difference between the maximum and minimum values of total energy in the process of Talbot self-imaging. Note that the total energy is normalized by the total energy of the incident pulses. We illustrate the oscillation amplitude E_{PO} varying with $|\phi_0|$ in Fig. 6(a). The oscillation amplitude increases almost exponentially with $|\phi_0|$ as the degree of nonorthogonality is enlarged. For $\phi_0 = 0.45\pi$, the Talbot distance is tuned to $z_T = 32$, as shown in Fig. 6(b) where slight power oscillations occur. For $\phi_0 = 0.87\pi$, the Talbot distance is $z_T = 60$, as illustrated in Fig. 6(c) where the oscillations are stronger than that in Fig. 6(b). The power oscillations, as unique features of the \mathcal{PT} -symmetric Talbot effect, could find applications in tunable intensity amplifiers. Compared to the fractional Talbot images in the passive systems, the pulse trains experience various degrees of amplification at different distances, through which the tunability of the amplification factor could be carried out. Moreover, the amplification factor can further be manipulated by controlling the gradient of the linear phase modulation.

C. Talbot effect above \mathcal{PT} transition threshold

The Talbot self-imaging even exists above the \mathcal{PT} transition threshold accompanied with dramatic power oscillations. For $N = 4$, the modes contained in the field evolution are excited at the center of the Brillouin zone. The propagation constant at the third band could also be denoted as Eq. (11). For $\gamma < \gamma_{IM}$, $\theta_{3,0}$ is a real number. Considering the symmetric

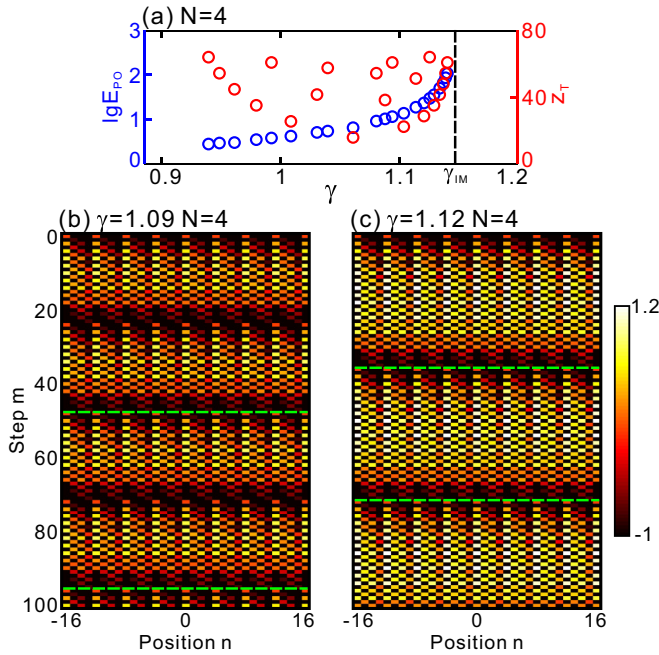


FIG. 7. (a) Talbot distance z_T and oscillation amplitude E_{PO} (after log transformation) varying with γ above the \mathcal{PT} transition threshold. The incident period is $N = 4$. (b), (c) Talbot carpets (after log transformation) for $\gamma = 1.09$ and 1.12 , respectively.

properties of band structure, $\theta_{1,0}$, $\theta_{2,0}$, and $\theta_{4,0}$ are all real numbers. The Talbot effect exists only if $\theta_{3,0}$ is a rational multiple of π . We denote $\theta_{3,0}$ as $p\pi/q$, and the Talbot distance is $z_T = 4q$. Due to $\pi/3 < \theta_{3,0} < \pi/2$, q is 4 at least. The set of available Talbot distances should thus be $\{16, 20, 24, \dots, 4q, \dots, M_L\}$. The power oscillations also exist in the Talbot process. As shown in Fig. 2(d), two EPs appear at the band structure, and they are approaching the center of the Brillouin zone with the increase of γ . Because the modes contained in the field evolution are excited at the center of the Brillouin zone, the degree of nonorthogonality is enlarged with the increase of γ . The oscillation amplitude is thus enlarged. We depict the Talbot distance z_T and oscillation amplitude E_{PO} varying with γ in Fig. 7(a). As $\gamma = 1.09$, the Talbot distance is tuned to $z_T = 48$ and the amplitude of the power oscillations is $E_{PO} = 10.37$. For $\gamma = 1.12$, the Talbot distance becomes $z_T = 36$, and the oscillation amplitude is $E_{PO} = 23.6$. We show the corresponding Talbot carpets in Figs. 7(b) and 7(c), which agree well with the above theoretic analysis. For $\gamma = \gamma_{IM}$, the EP lies at the center of the Brillouin zone. The total energy increases almost linearly along the propagation direction, leading to the failure of the Talbot effect. As $\gamma > \gamma_{IM}$, the band structure is completely complex. As shown in Fig. 2(f), the modes contained have the propagation constants with different imaginary parts. The input field distribution is impossible to recover as these modes experience various degrees of amplification or attenuation. Therefore, the Talbot effect will not be preserved as the modes contained are excited at the complex zone of the band structure. For $N > 4$, we also employ the enumeration method to discuss the existence of the Talbot effect. As a result, the Talbot recurrence disappears.

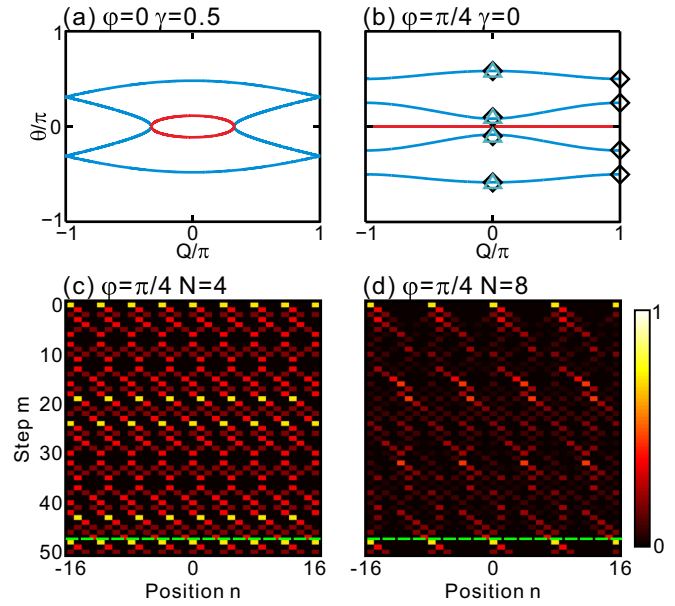


FIG. 8. (a) Band structures for $\varphi = 0$ and $\gamma = 0.5$. (b) Band structure for $\varphi = \pi/4$ and $\gamma = 0$. The modes contained in the field evolution for $N = 4$ and 8 are represented as the cyan triangles and black diamonds, respectively. (c), (d) Talbot carpets for $N = 4$ and 8 , respectively. φ and γ are chosen as $\pi/4$ and 0 , respectively.

D. Other modulation phase φ

We now provide a brief discussion of the Talbot effect with other modulation phase φ . For $\varphi = 0$ or π , the band structure becomes

$$\cos Q = 8 \cos^2 \theta - 8 \cosh \gamma \cos \theta + \cosh(2\gamma). \quad (18)$$

As $\gamma = 0$, the Talbot effect only exists for $N = 2, 4$, or 8 , which has been studied in the previous work [45]. The corresponding Talbot distances are $z_T = 8, 8$, and 24 , respectively. Note that both the phase modulation and the gain and loss vanish in such cases. As $\gamma > 0$, the imaginary part of the propagation constant is nonzero at the center of the Brillouin zone [Fig. 8(a)]. For arbitrary choice of N , the modes with $Q = 0$ are contained in the field evolution necessarily. As a result, the Talbot effect will not be supported. For $\varphi = \pm\pi/4$, the band structure reads

$$\cos Q = 8 \cos^2 \theta - 4\sqrt{2} \cosh \gamma \cos \theta - 2 + \cosh(2\gamma). \quad (19)$$

The Talbot effect occurs only if $\gamma = 0$, which is obtained through the enumeration method. For $N = 4$, the propagation constants are $\theta_{1,0} = -7\pi/12$, $\theta_{2,0} = -\pi/12$, $\theta_{3,0} = -\pi/12$, and $\theta_{4,0} = 7\pi/12$, as illustrated in Fig. 8(b). The corresponding revival distances are all 48, leading to the Talbot distance of $z_T = 48$. For $N = 8$, the Talbot distance is also $z_T = 48$ as the set of propagation constants is $\{\pm\pi/12, \pm\pi/4, \pm\pi/2, \pm7\pi/12\}$ [Fig. 8(b)]. The Talbot effect is not supported for other input periods. The Talbot carpets shown in Figs. 8(c) and 8(d) agree well with the above theoretical analysis. As $\varphi = 3\pi/4$ or $-3\pi/4$, the Talbot self-imaging also only exists under the same conditions, and the Talbot distance is $z_T = 48$.

Finally, an experimental proposal is suggested. The input pulse sequence comes from a mode-locked laser and possesses a repetition rate of 5 GHz. Through an optical switch driven by an arbitrary waveform generator (AWG), the pulse train is injected to the fiber loop. The time delays of the fiber loops are about tens of nanoseconds. By inserting an optical delay line in the long loop, the time interval between two fiber loops could be adjusted precisely. The gain, which is the requirement of \mathcal{PT} symmetry, is provided by erbium-doped optical fibers (EDFs). By employing a Mach-Zehnder intensity modulator (MZM) driven by AWG, the temporal control of the gain and loss is realized in each loop. Considering the time delays of the fiber loops, the switch between gain and loss should have a speed of dozens of MHz. Moreover, it does not require a very sharp change between gain and loss. The switch begins after the pulse train quits the MZM. Before the sequence enters the MZM again, the MZM could have enough time to accomplish the switch between gain and loss, i.e., at the nanosecond level. The phase modulation is accomplished by a phase modulator (PM), which is also driven by the AWG. All of the modulators and AWGs should possess a bandwidth of ~ 10 GHz. The pulse trains can be coupled out from the coupled loops through optical switches and detected by the photodiodes (PDs). In addition, the insertion loss caused by these devices can be compensated by the EDFs.

IV. CONCLUSIONS

In conclusion, we investigate the \mathcal{PT} -symmetric Talbot effect in the temporal mesh lattice constructed by the two coupled fiber loops. We expand on the Talbot recurrence below, at, and above the \mathcal{PT} transition threshold. The Talbot self-imaging exists only for an incident period of $N = 4$ or 8. The Talbot distance could be flexibly manipulated by controlling the gain and loss or imposing a linear phase modulation on the input pulse train. The set of available Talbot distances is $\{12, 16, 20, \dots, 4q, \dots, M_L\}$, where q is a positive integer, and M_L is the longest valid propagation distance. Additionally, significant power oscillations exist in the Talbot process as the modes are excited near the EPs, and the oscillation amplitude could be controlled through varying the gain and loss and the gradient of the linear phase modulation. The study may find great applications in pulse repetition rate multiplication, temporal cloaking, and tunable intensity amplifiers.

ACKNOWLEDGMENTS

The work is supported by the 973 Program (Program No. 2014CB921301) and the National Natural Science Foundation of China (Grant No. 11674117).

-
- [1] C. M. Bender and S. Boettcher, *Phys. Rev. Lett.* **80**, 5243 (1998).
 - [2] C. M. Bender, D. C. Brody, and H. F. Jones, *Phys. Rev. Lett.* **89**, 270401 (2002).
 - [3] K. G. Makris, R. El-Ganainy, D. N. Christodoulides, and Z. H. Musslimani, *Phys. Rev. Lett.* **100**, 103904 (2008).
 - [4] Z. H. Musslimani, K. G. Makris, R. El-Ganainy, and D. N. Christodoulides, *Phys. Rev. Lett.* **100**, 030402 (2008).
 - [5] A. Guo, G. J. Salamo, D. Duchesne, R. Morandotti, M. Volatier-Ravat, V. Aimez, G. A. Siviloglou, and D. N. Christodoulides, *Phys. Rev. Lett.* **103**, 093902 (2009).
 - [6] S. Longhi, *Phys. Rev. Lett.* **103**, 123601 (2009).
 - [7] C. E. Rüter, K. G. Makris, R. El-Ganainy, D. N. Christodoulides, M. Segev, and D. Kip, *Nat. Phys.* **6**, 192 (2010).
 - [8] M. C. Zheng, D. N. Christodoulides, R. Fleischmann, and T. Kottos, *Phys. Rev. A* **82**, 010103 (2010).
 - [9] Z. Hong, S. A. Rezvani, Q. Zhang, and P. Lu, *Opt. Quantum Electron.* **49**, 392 (2017).
 - [10] Z. Hong, Q. Zhang, S. A. Rezvani, P. Lan, and P. Lu, *Opt. Laser Technol.* **98**, 169 (2018).
 - [11] Z. Lin, H. Ramezani, T. Eichelkraut, T. Kottos, H. Cao, and D. N. Christodoulides, *Phys. Rev. Lett.* **106**, 213901 (2011).
 - [12] L. Feng, Y. L. Xu, W. S. Fegadolli, M. H. Lu, J. E. Oliveira, V. R. Almeida, Y. F. Chen, and A. Scherer, *Nat. Mater.* **12**, 108 (2013).
 - [13] L. Feng, R. El-Ganainy, and L. Ge, *Nat. Photonics* **11**, 752 (2017).
 - [14] D. Zhao, W. Liu, S. Ke, and Q. Liu, *Opt. Quantum Electron.* **50**, 323 (2018).
 - [15] A. A. Zyablovsky, A. P. Vinogradov, A. A. Pukhov, A. V. Dorofeenko, and A. A. Lisiansky, *Phys.-Usp.* **57**, 1063 (2014).
 - [16] C. Qin, F. Zhou, Y. Peng, D. Sounas, X. Zhu, B. Wang, J. Dong, X. Zhang, A. Alù, and P. Lu, *Phys. Rev. Lett.* **120**, 133901 (2018).
 - [17] S. Wang, B. Wang, C. Qin, K. Wang, H. Long, and P. Lu, *Opt. Quantum Electron.* **49**, 389 (2017).
 - [18] M.-A. Miri, A. Regensburger, U. Peschel, and D. N. Christodoulides, *Phys. Rev. A* **86**, 023807 (2012).
 - [19] A. Regensburger, C. Bersch, M. A. Miri, G. Onishchukov, D. N. Christodoulides, and U. Peschel, *Nature* **488**, 167 (2012).
 - [20] I. D. Vatnik, A. Tikan, G. Onishchukov, D. V. Churkin, and A. A. Sukhorukov, *Sci. Rep.* **7**, 4301 (2017).
 - [21] M. Hou, Y. Wang, S. Liu, Z. Li, and P. Lu, *IEEE Sens. J.* **16**, 6192 (2016).
 - [22] A. Regensburger, M. A. Miri, C. Bersch, J. Nager, G. Onishchukov, D. N. Christodoulides, and U. Peschel, *Phys. Rev. Lett.* **110**, 223902 (2013).
 - [23] C. Qin, B. Wang, and P. Lu, *Opt. Express* **26**, 25721 (2018).
 - [24] Q. Liu, S. Ke, and W. Liu, *Opt. Quantum Electron.* **50**, 356 (2018).
 - [25] L. Li, P. Lan, X. Liu, L. He, X. Zhu, O. D. Mücke, and P. Lu, *Opt. Express* **26**, 23844 (2018).
 - [26] M. Wimmer, M. A. Miri, D. Christodoulides, and U. Peschel, *Sci. Rep.* **5**, 17760 (2015).
 - [27] L. Yuan, Y. Shi, and S. Fan, *Opt. Lett.* **41**, 741 (2016).
 - [28] T. Ozawa, H. M. Price, N. Goldman, O. Zilberberg, and I. Carusotto, *Phys. Rev. A* **93**, 043827 (2016).
 - [29] L. Yuan, Q. Lin, M. Xiao, A. Dutt, and S. Fan, *APL Photonics* **3**, 086103 (2018).
 - [30] H. F. Talbot, *Philos. Mag.* **9**, 401 (1836).
 - [31] L. Rayleigh, *Philos. Mag.* **11**, 196 (1881).
 - [32] J. T. Winthrop and C. R. Worthington, *J. Opt. Soc. Am.* **55**, 373 (1965).

- [33] K. Patorski, *Prog. Opt.* **27**, 1 (1989).
- [34] M. V. Berry and S. Klein, *J. Mod. Opt.* **43**, 2139 (1996).
- [35] T. Jansson and J. Jansson, *J. Opt. Soc. Am.* **71**, 1373 (1981).
- [36] B. H. Kolner, *IEEE J. Quantum Electron.* **30**, 1951 (1994).
- [37] J. Azaña and M. A. Muriel, *Opt. Lett.* **24**, 1672 (1999).
- [38] J. Azaña and M. A. Muriel, *Appl. Opt.* **38**, 6700 (1999).
- [39] S. Longhi, M. Marano, P. Laporta, O. Svelto, M. Belmonte, B. Agogliati, L. Arcangeli, V. Pruneri, M. N. Zervas, and M. Ibsen, *Opt. Lett.* **25**, 1481 (2000).
- [40] J. Azaña and M. A. Muriel, *IEEE J. Sel. Top. Quantum Electron.* **7**, 728 (2001).
- [41] J. M. Lukens, D. E. Leaird, and A. M. Weiner, *Nature* **498**, 205 (2013).
- [42] J. M. Lukens, A. J. Metcalf, D. E. Leaird, and A. M. Weiner, *Optica* **1**, 372 (2014).
- [43] B. Li, X. Wang, J. Kang, Y. Wei, T. Yung, and K. K. Y. Wong, *Opt. Lett.* **42**, 767 (2017).
- [44] R. Maram, J. Van Howe, M. Li, and J. Azaña, *Nat. Commun.* **5**, 5163 (2014).
- [45] S. Wang, C. Qin, B. Wang, and P. Lu, *Opt. Express* **26**, 19235 (2018).
- [46] R. Iwanow, D. A. May-Arrijoja, D. N. Christodoulides, G. I. Stegeman, Y. Min, and W. Sohler, *Phys. Rev. Lett.* **95**, 053902 (2005).
- [47] Y. Wang, K. Zhou, X. Zhang, K. Yang, Y. Wang, Y. Song, and S. Liu, *Opt. Lett.* **35**, 685 (2010).
- [48] F. Wang, C. Qin, B. Wang, H. Long, K. Wang, and P. Lu, *IEEE J. Sel. Top. Quantum Electron.* **23**, 4600105 (2017).
- [49] Y. Fan, B. Wang, K. Wang, H. Long, and P. Lu, *Opt. Lett.* **39**, 3371 (2014).
- [50] Z. Wang, B. Wang, H. Long, K. Wang, and P. Lu, *J. Lightwave Technol.* **35**, 2960 (2017).
- [51] K. Li, F. Xia, M. Wang, P. Sun, T. Liu, W. Hu, W. Kong, M. Yun, and L. Dong, *Carbon* **118**, 192 (2017).
- [52] F. Wang, S. Ke, C. Qin, B. Wang, H. Long, K. Wang, and P. Lu, *Opt. Laser Technol.* **103**, 272 (2018).
- [53] S. Ke, D. Zhao, Q. Liu, S. Wu, B. Wang, and P. Lu, *J. Lightwave Technol.* **36**, 2510 (2018).
- [54] H. Ramezani, D. N. Christodoulides, V. Kovanis, I. Vitebskiy, and T. Kottos, *Phys. Rev. Lett.* **109**, 033902 (2012).
- [55] S. Ke, B. Wang, H. Long, K. Wang, and P. Lu, *Opt. Quantum Electron.* **49**, 224 (2017).
- [56] S. Ke, B. Wang, C. Qin, H. Long, K. Wang, and P. Lu, *J. Lightwave Technol.* **34**, 5258 (2016).